1.5 Observations and numerical simulations of the diurnal cycle of the EUROCS stratocumulus case *

Stephan R. de Roode
Institute for Marine and Atmospheric Research Utrecht, University of Utrecht, The Netherlands

1. Introduction

The presence of a stable temperature inversion at the top of the atmospheric boundary layer, and the availability of sufficient moisture are the major ingredients for the formation and maintenance of stratocumulus clouds. Extended marine stratocumulus-topped boundary layers (STBLs) are therefore frequently found above the subtropical oceans in the descending branches of the Hadley circulation (Klein and Hartmann, 1993; Norris, 1997a,b). Figure 1 shows a striking example of a solid stratocumulus deck above the Pacific Ocean off the coast of California, and clear skies over the continent. Due to its high albedo, stratocumulus clouds strongly diminish the solar insolation of the Earth's surface during daytime. On the other hand, stratocumulus clouds are often sufficiently optically thick such that longwave radiation is emitted as a black body just like the underlying ocean surface. These radiative properties make stratocumulus an important factor in determining the Earth's surface energy balance.

The EUROpean Cloud Systems (EUROCS) project used observations collected in stratocumulus-topped boundary layers off the coast of California during FIRE I (Hignett, 1991; Duynkerke and Hignett, 1993) as a basis to set up a well-defined modeling case for the diurnal cycle of stratocumulus. The modeling results can be compared to observations of cloud cover, liquid water path, cloud base and cloud top height, downwelling shortwave radiation at the surface, and the turbulence structure of the boundary layer. The EUROCS stratocumulus case includes simulations with six large-eddy simulation (LES) and ten single-column models, the results of which are reported in detail in Duynkerke et al. (2004).

In this paper we will consider the LES results to address the following questions:

- What is the typical accuracy needed for entrainment rate parameterizations?
- What is the effect of the development of mesoscale structures on the PDF of the liquid water path?

2. Model initialization

The FIRE I stratocumulus experiment performed off the coast of southern California in July 1987 provides a very comprehensive set of data on marine stratocumulus from airborne, ground-based and satellite instruments (Albrecht et al., 1988). Several instruments were installed on San Nicolas island, approximately $33^\circ 15' N$ and $119^\circ 30' W$, to monitor cloud properties with a high temporal resolution. In addition, Hignett (1991) and Duynkerke and Hignett (1993) present the turbulence structure in the boundary layer as measured on 14 and 15 July 1987 by means of an instrumented tethered balloon.

The boundary-layer structure observed from four radiosondes during 14 July is is shown in Figure 2, in addition to the mean structure as determined from sixty-nine radiosonde soundings made during 1 to 19 July 1987. The mean potential temperature in the boundary layer compares well with the individual soundings from 14 July, though the mean specific humidity is a bit lower. The initial vertical profiles used in the models are indicated by the thick solid lines in Figure 2. An explanation of the specification of the selected initial inversion jumps, the treatment of radiation and the prescribed large-scale forcing can be found in the Appendix.

Since the initial state is reasonably close to the radiosonde soundings during 14 and 15 July, we will

*Corresponding author address: Stephan R. de Roode, Institute for Marine and Atmospheric Research Utrecht (IMAU), Princetonplein 5, 3584 CC Utrecht, The Netherlands. Email: roode@phys.uu.nl

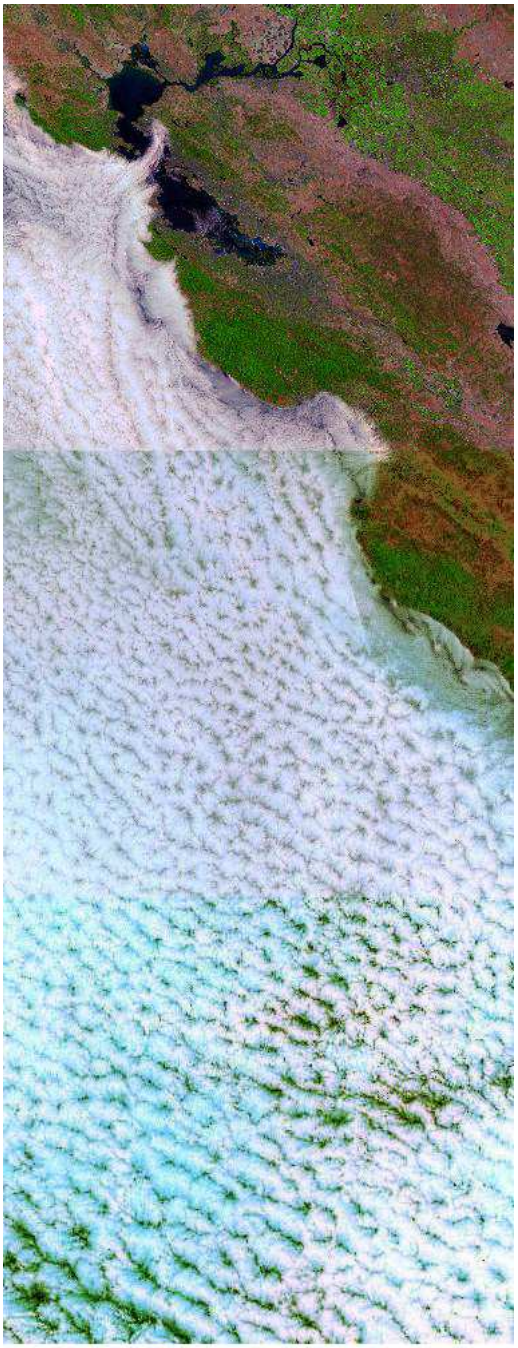

Figure 1: Landsat satellite image (domain size about 200 by 600 km^2) showing stratocumulus off the coast of California for 14 July 1987. The cloud tops are at about 500 $\sim$ 1000 m whereas the convective cells have a horizontal dimension of about 10 km. The aspect ratio of the convective cells is thus much larger than one.

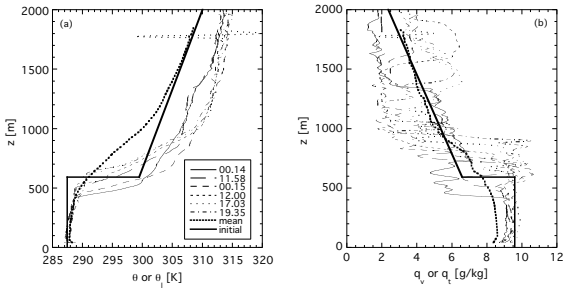

Figure 2: The observed vertical profiles of the a) potential temperature θ and the b) specific humidity q_v at 0014 and 1158 UTC 14 July and 0015, 1200, 1703 and 1935 UTC 15 July. The mean of the observed profiles collected between 1 and 19 July 1987 is indicated by the thick dashed line. The thick solid lines are the initial conditions for the liquid water potential temperature (θ_l) and total water content (q_t) prescribed in the models. The linestyles are according to the legend displayed in the left panel.

compare the model results with observations from this period. The model simulations start at 14 July 0800 UTC (= 0000 h Local Time (LT)) and last at least 37 hours. Since the monthly-mean atmospheric state does not differ very much from the initial profiles either, we will present monthly-mean values of the observations, too.

3. Turbulence structure

The turbulence observations collected by means of a tethered balloon during FIRE I, discussed in detail by Hignett (1991), facilitate a comparison with the results obtained from 6 LES models (UKMO, NCAR, IMAU, WVU, MPI and INM). In particular, we will consider the vertical velocity variance ($\overline{w'w'}$) and the buoyancy flux $B = \frac{g}{\theta_0}\overline{w'\theta_v'}$, with g the acceleration due to gravity, and $\theta_0 \approx 300K$ a reference temperature. The observations and the LES results are presented for both night-time and daytime in Figure 3. The LES results are in a good qualitative agreement with the observations and fall within the range of scatter in the observations, although the vertical velocity variance during night-time seems to be slightly overpredicted by most of the LES models. It can be concluded that the LES models are all capable of reproducing the observed turbulence structure during the

diurnal cycle fairly well.

Clearly, there are distinct differences in the turbulence structure during daytime and night-time. During the night longwave radiative cooling near cloud top is the dominant process that drives the turbulent mixing throughout the boundary layer. In addition, latent heat release effects support a positive buoyancy flux in the cloud layer. The maximum vertical velocity variance is located in the upper half of the boundary layer. During the day the effect of shortwave radiative absorption in the cloud layer becomes manifest. The shortwave radiative warming of the cloud layer leads to a significant reduction of the buoyancy flux. The slightly negative buoyancy fluxes in the middle of the boundary layer tend to damp the vertical turbulent motions leading to a minimum vertical velocity variance near the middle of the boundary layer. This vertical velocity variance profile characterizes a decoupled boundary layer and indicates that the moist turbulent eddies driven from the surface cannot reach the cloud layer anymore. Because entrainment maintains a steady supply of relatively warm and dry air from above the inversion into the cloud layer, the cloud layer tends to thin during daytime, as clearly illustrated from the LWP evolution shown in Figure 4. Because decoupling leads to different heating and moistening rates in the sub-cloud and cloud layer, conserved quantities like θ_l and q_t can not be maintained in a vertically well-mixed state anymore.

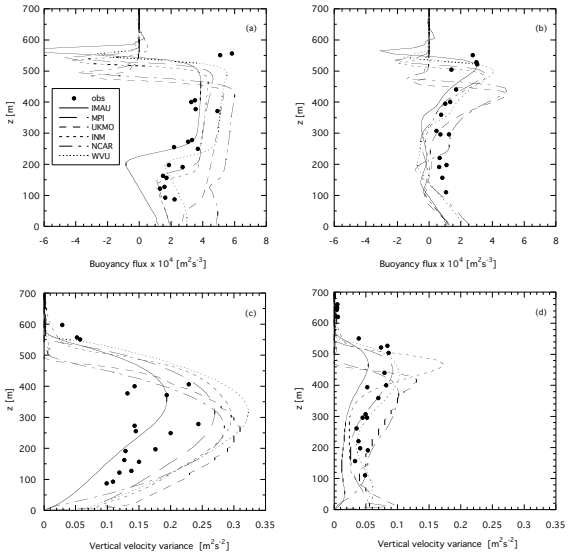

Figure 3: Vertical profiles of observations and LES results. a) Buoyancy flux during a) night-time, b) daytime, and the vertical velocity variance during c) night-time and d) daytime. Note that the LES results represent hourly averaged values between $2300 \leq t < 2400h$ (night-time) and $3500 \leq t < 3600h$ LT (daytime). The linestyles are according to the legend displayed in the upper left panel.

4. Entrainment

In Figure 4 the LWPs from the LES models are compared to the retrievals of the microwave radiometer from 14 and 15 July 1987, and the hourly monthly-mean diurnal variation. All the LESs capture the strong diurnal variation in LWP due to the forcing imposed by the shortwave heating on the cloud layer. Like the observations, the maximum cloud thickness is found during the night, and the cloud deck gradually thins until noon. However, the thinning is not sufficient to break up the cloud; in all the LESs the cloud cover remains equal to unity. After 30 hours of simulation time the difference between the minimum (IMAU) and maximum (UKMO) values for the modeled LWP ranges by nearly a factor of two. This variation is about as large as the difference between the monthly mean and observed diurnal cycle. Note that the LWP is very sensitive to small changes in the

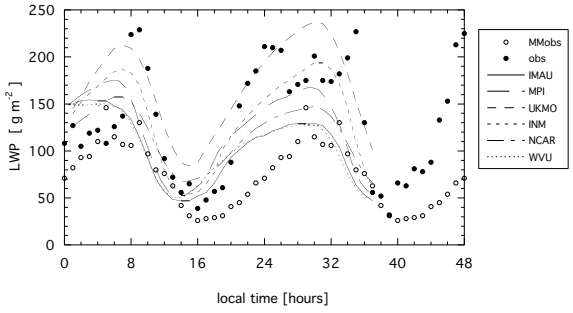

Figure 4: The observed and modeled LWP from six different LES models as a function of time for 14 and 15 July 1987 (denoted from 0 to 48 hours Local Time). The filled dots are the hourly mean observed values (obs) whereas the open circles are the hourly monthly-mean values (MMobs). The linestyles (LES results) are according to the legend.

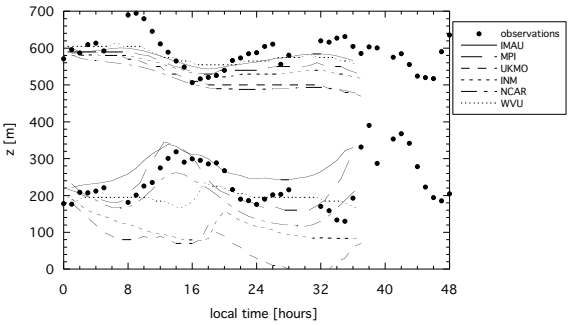

Figure 5: The cloud-base and cloud-top height from observations and Large-Eddy Simulations as a function of time for 14 and 15 July 1987 (denoted from 0 to 48 hours Local Time). The linestyles are according to the legend.

thermodynamic structure of the boundary layer. If the boundary layer is vertically well-mixed then the liquid water content q_l increases approximately linearly with height and consequently (Albrecht et al., 1990)

$$LWP \propto (c_t - c_b)^2, \tag{1}$$

where c_t and c_b represent the cloud-top and cloud-base heights. As an example, for the EUROCS stratocumulus case this implies that for a cloud layer that is 350 m thick, a change of just 20 m leads to a subsequent variation in the LWP of nearly 12%.

Figure 5 compares the modeled cloud-base and cloud-top height evolution to the observations. The top of a stratocumulus cloud layer is usually located just below the inversion height z_i, the latter of which varies with time according to

$$\frac{dz_i}{dt} = \overline{w}(z_i) + w_e. \tag{2}$$

An inspection of the cloud-top height evolution therefore gives a good appreciation of differences in the entrainment rate. After 37 hours simulation time the typical scatter in the cloud-top heights is about 100 m. Such a variation corresponds roughly with a typical difference in the mean entrainment rate on the order of $1\,mm\,s^{-1}$. The differences in the cloud layer depth are mainly due to variations in the simulated cloud-base height. The lowest cloud bases are due to larger moistening rates of the boundary layer, and are found for models that simulate the smallest entrainment rates. There is a much larger amplitude in the observed cloud-top height during the first diurnal cycle than in the simulations. Possibly, a diurnal cycle in the subsidence rate may play a role, as was found from an observational study of stratocumulus over the southeast Pacific region (Bretherton et al., 2004).

The entrainment rates from the LES models shown in Figure 6 were diagnosed by applying the tendency equation (2) for the boundary layer depth z_i. The inversion height z_i is determined from the level where $q_t = 8.1g\,kg^{-1}$, obtained by linear interpolation between adjacent grid levels of total water content. Figure 6 shows that there is a clear diurnal cycle in the entrainment rate. Minimum values are found for the daytime period when the buoyancy flux is minimal, and the mean entrainment rate from the six LES results is $w_e = 0.36 \pm 0.03cm\,s^{-1}$, for $1100 \leq t < 1400h$ LT. During night-time ($0100 \leq t < 0400h$ LT) the mean entrainment rate is larger, $w_e = 0.58 \pm 0.08cm\,s^{-1}$.

A mixed-layer model was utilized to compute the budgets for heat and moisture during the night (Nicholls, 1984). This model assumes that in the boundary layer the tendency for $\overline{\theta_l}$ does not depend on the height and is given by

$$\frac{\partial \overline{\theta_l}}{\partial t} = \frac{w_e \Delta \overline{\theta_l} + \overline{w'\theta'_l}_0}{z_i} + \left\langle \frac{\partial \overline{\theta_l}}{\partial t} \right\rangle_{LS} + \langle S_{\theta_l} \rangle, \tag{3}$$

where the operator $\langle\,\rangle$ gives the vertical mean value for any arbitrary function $f(z)$,

$$\langle f \rangle = \frac{\int_0^{z_i} f(z) dz}{z_i}, \tag{4}$$

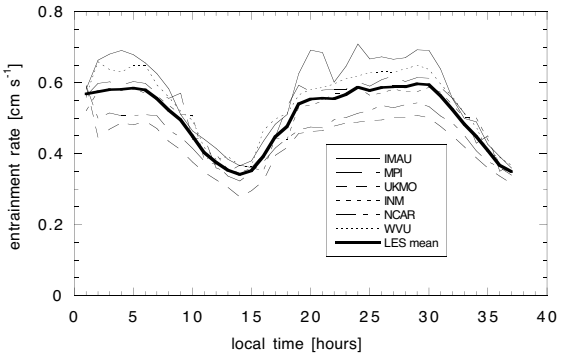

Figure 6: LES results of the entrainment rate as a function of time. In addition, the mean entrainment rate from all LESs is shown. The linestyles are according to the legend.

and S_{θ_l} is a source term that can represent, for example, the tendency due to a physical process like radiation. The tendency for the total water content is computed similar to (3). If a different heating rate occurs in the sub-cloud layer than in the cloud layer, a situation typically encountered in a decoupled boundary layer during daytime, the mixed layer model cannot be applied. The large-scale forcings like horizontal advection and the longwave radiative flux divergence were computed in accordance with the case set-up, Eqs. (12) and (13). The LES results were used as input for the turbulent fluxes at the surface and for the entrainment rate at the boundary layer top. From all the LES model results we computed mean values representative for the nighttime period, $0100 \leq t < 0400h$ LT. For the turbulent surface fluxes of heat and moisture we obtained $H = 9.5 \pm 6.4 Wm^{-2}$, $LE = 31.7 \pm 5.1 Wm^{-2}$.

The results presented in Table 1 indicate that entrainment causes the largest tendencies for both moisture and heat. Note that although the longwave radiative flux divergence causes a significant cooling, the application of Eq. (13) gives about the same cooling rate for all LES models since the stratocumulus cloud layers are sufficiently optically thick during the entire diurnal cycle. Thus, we conclude that the differences in the entrainment rate among the LES models are the primary source for the variations in the simulated LWP evolution during night-time. During the night, a larger entrainment rate causes smaller LWPs, and vice versa.

	$\frac{\partial \theta_l}{\partial t}$	$\frac{\partial \overline{q}_t}{\partial t}$
surface flux	0.05 ± 0.03	0.067 ± 0.011
entrainment	0.42 ± 0.06	-0.105 ± 0.015
ls adv	-0.14	0.055
longwave rad	-0.37	

Table 1: The contribution of the surface fluxes, entrainment, large-scale horizontal advection (ls adv) and longwave radiation to the tendencies of the liquid water potential temperature $[K\ hr^{-1}]$ and the total specific humidity $[(g\ kg^{-1})\ hr^{-1}]$ in the boundary layer. The mean values and standard errors were computed from all the LES results during the nighttime period $0100 \leq t < 0400h$ LT. Recall that the large-scale advection and longwave radiation were prescribed in the models.

5. LES on a large horizontal domain

a. Production of variance

The satellite image shown in Figure 1 reveals that the stratocumulus cloud field is dominated by mesoscale structures, a phenomenon that was also frequently observed from aircraft during FIRE I (Moyer and Young, 1994). Recently, Jonker et al. (1999) demonstrated by an large-eddy simulation of the *dry* penetrative convective boundary layer (mixed layer capped by an inversion) that passive scalar (inert tracer) fields appear to undergo significant cell broadening. To investigate the role of the horizontal domain on the development of mesoscale fluctuations in the stratocumulus-topped boundary layer a few additional large-eddy simulations were performed on different domain horizontal sizes. First, simulations were performed for 4 different domain sizes, namely 3.2 km, 6.4 km, 12.8 km and 25.6 km. These simulations lasted 8 hours and the shortwave radiation was turned off. Second, the entire diurnal cycle was simulated on a horizontal domain size of 25.6 km. The horizontal resolution for these additional simulations was 100 m.

Figure 7a shows that the largest fluctuations in the vertical wind velocity spectrum are present at scales in the vicinity of the boundary layer depth. Moreover, the spectral energy rapidly decreases towards larger length scales (smaller wavenumbers). The fact that the spectral energy in the vertical component of

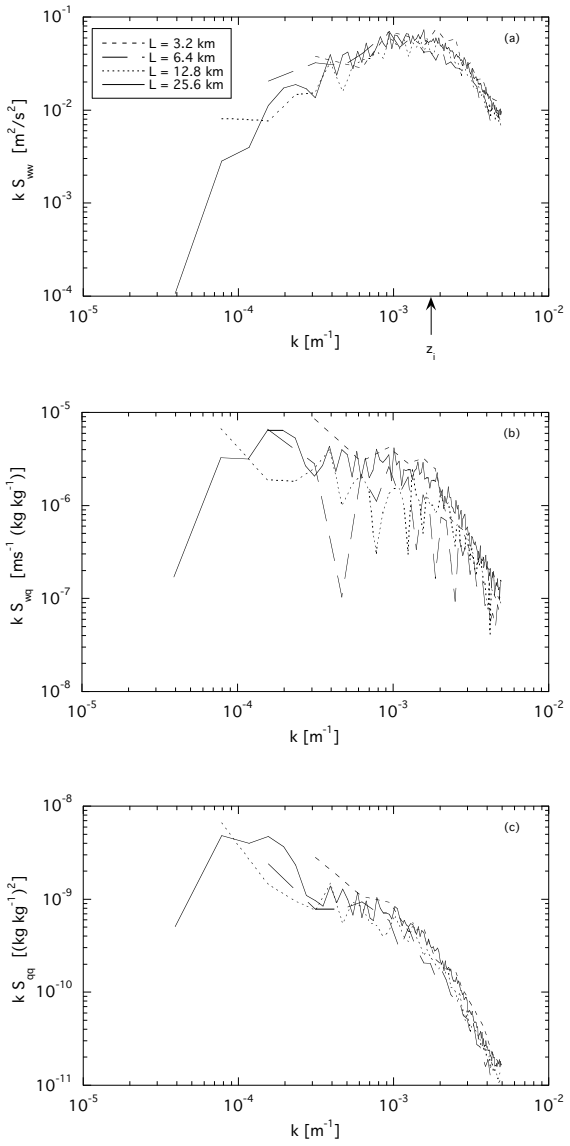

Figure 7: (Co-)variance spectrum S multiplied by the wavenumber k just above the stratocumulus cloud base ($z/z_i = 0.6$) for four different domain sizes (L). (a) The vertical velocity w, (b) the vertical flux of the total specific humidity and (c) the total specific humidity q_t. Linestyles are according to the legend in the upper panel. The wavenumber corresponding to the reciprocal of the boundary layer depth z_i is indicated by the vertically pointing arrow.

the wind does not vanish, i.e. has a nonzero value at the largest wavelengths, does explain the presence of mesoscale fluctuations in the total water content spectrum. This can be understood by considering the first term on the right-hand-side (rhs) of the equation for the perturbation for an arbitrary, conserved variable ψ' (Stull, 1988),

$$\frac{\partial \psi'}{\partial t} = -u_j' \frac{\partial \overline{\psi}}{\partial x_j} - u_j' \frac{\partial \psi'}{\partial x_j} + \nu_\psi \frac{\partial^2 \psi'}{\partial x_j^2} + \frac{\partial \overline{u_j' \psi'}}{\partial x_j}, \quad (5)$$

where we neglected the contribution of the mean wind for notational convenience. Thus for $j = 3$ the production rate of ψ-fluctuations depends on the magnitude of the vertical gradient for the mean, $\frac{\partial \overline{\psi}}{\partial z}$, and the magnitude of the vertical velocity fluctuations, w'. Note that for the spectral space an identical argument is applicable. Eq. (5) can be used to derive a prognostic equation for the Reynolds-averaged variance,

$$\frac{\partial \overline{\psi' 2}}{\partial t} = -2\overline{w'\psi'} \frac{\partial \overline{\psi}}{\partial z} - \frac{\partial \overline{w'\psi'\psi'}}{\partial z} - \epsilon_\psi, \quad (6)$$

with on the rhs of the equation the production, transport, and dissipation term, respectively. In the LES model the total specific humidity spectrum clearly exhibits fluctations at the mesoscales, which is produced by the vertical flux at these scales (Figure 7b and c).

b. Liquid water path distribution

Cahalan and Snider (1989) analysed observations of the microwave radiometer installed on San Nicholas Island during FIRE I and found that the vertically integrated liquid water content exhibits a -5/3 power law up to horizontal length scales well above 100 km. Such mesoscale variations give rise to errors in radiative transfer computations that assume a horizontally homogeneous cloud layer. A horizontally varying liquid water field will decrease the mean albedo compared to a horizontally uniform field, since the albedo of optically thick regions saturates as the optical depth is increased (Cahalan et al., 1994).

Figure 8 shows the LWP fields at two different domain sizes after 8 hours of simulation time. Despite the fact that the mean LWPs do not differ very much, the cloud structures appear remarkably different and it appears that the small horizontal domain size acts to limit the growth of mesoscale cloud cells.

For the purpose of radiative transfer computations, the probability density function for the liquid-water

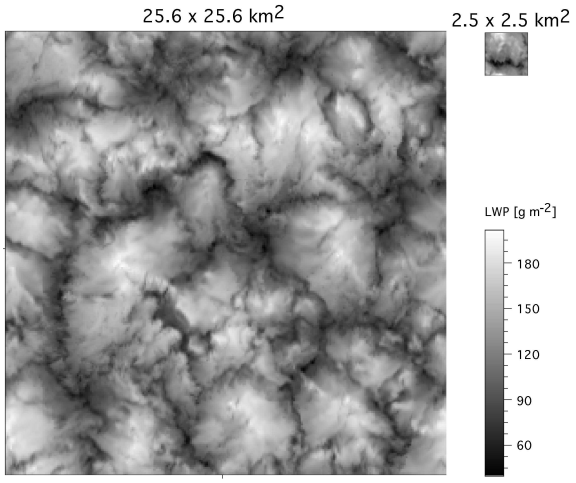

Figure 8: The LWP field at $t = 0800\ h$ LT from the IMAU LES at the standard domain size ($2.5 \times 2.5km^2$) and at a large horizontal domain size ($25.6 \times 25.6km^2$).

path fluctuations, $P(LWP')$, is the relevant quantity to consider (Cahalan et al., 1994). Figure 9 shows $P(LWP')$ for the small and large domain simulations, in addition to $P(q_t')$, which is relevant for microphysical computations (Wood and Field, 2000). Clearly, the PDFs depend on the horizontal domain size. The simulation at the small domain has relatively more columns that have a LWP close to the mean value, whereas the large domain allows for a broader LWP distribution. A similar distribution is found for the total water content in the middle of the cloud layer. Figure 7 illustrates that although a small domain size may be sufficient to represent the vertical motions that have a spectral peak at scales on the order of the boundary layer depth, this is not necessarily the case for quantities like the total specific humidity, for which fluctuations tend to grow at much larger scales. If these fluctuations cannot be properly represented by a too small domain, the variance of the quantity will be underestimated. For the PDFs shown in the Figure 9b, the q_t variance is about a factor of two smaller in the small domain simulation, whereas the LWP variance is 812 and 514 $(g\,m^{-2})^2$ for the large and small domain simulations, respectively.

Los and Duynkerke (2001) investigated the effect of horizontal cloud inhomogeneities on the mean albedo using the Independent Pixel Approximation. They applied a Taylor expansion to conclude that the

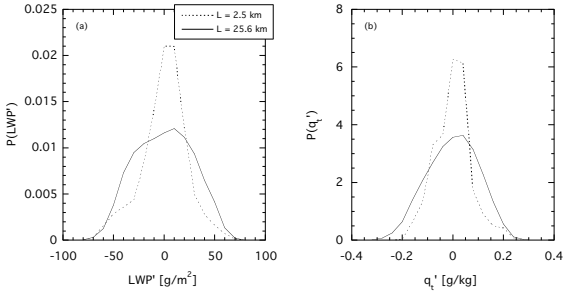

Figure 9: The probability density function P for a) the LWP and b) the total specific humidity fluctuations in the middle of the cloud layer at $t = 0800h$ LT. The two lines represent results from two large-eddy simulations on a small ($L = 2.5 \times 2.5km^2$) and a large horizontal domain ($L = 25.6 \times 25.6km^2$), respectively. The line styles are as indicated by the legend.

albedo bias is mainly determined by the variance of the cloud optical depth. This implies that given the same mean value for the LWP, a larger variance for the LWP will effectively lead to a reduction of the mean albedo.

6. Conclusions

The diurnal cycle of stratocumulus off the coast of California has been simulated by 6 different LES models. Large-scale forcings like advection are prescribed or computed from identical routines (like shortwave and longwave radiation). Differences in the evolution of the cloud layer must therefore be attributed entirely to differences in the surface and entrainment fluxes of heat and moisture.

• The contribution to the tendencies of the means for the total water content and the liquid water potential temperature in the boundary layer is dominated by entrainment. As the typical differences in the entrainment rate are relatively small, namely on the order of 1 mm/s, one can conclude that the LES models agree rather well in this respect.

• Small differences in the entrainment rate cause variations in the modeled cloud-top heights of about 100 m after 37 hours simulation time.

• The liquid water path is a quantity that is very sensitive to the cloud depth. Relatively small differences in the surface and entrainment fluxes of heat and moisture can lead to differences in the liquid wa-

ter path by as much as a factor of 2.

• If the horizontal domain size of the LES model is increased to $25 \times 25 km^2$, cloud cell sizes obtain mesoscale fluctuations, which is in accord with satellite observations.

• As a consequence of the development of mesoscale fluctuations, the PDF of the liquid water path and the total specific humidity is found to broaden.

This paper has summarized the major findings of three recent papers. The results of the EUROCS stratocumulus comparison case is reported by Duynkerke et al. (2004), and includes a discussion on the results of single-column models. De Roode et al. (2004a) explain the role of the horizontal domain size on the development of mesoscale fluctuations for a clear convective boundary layer, a smoke cloud case, and the EUROCS stratocumulus case. The length scales (as determined from Fourier spectra) for various conserved variables in these boundary layers appear to be systematically smaller if their vertical flux changes sign in the boundary layer, i.e. in cases for which the entrainment flux has an opposite sign to the surface flux. De Roode et al. (2004b) demonstrate that if the flux changes sign, vertical layers in which the flux is countergradient are usually present. This is simply due to the fact that the mean vertical gradient of the quantity under consideration generally changes sign at another level than does its vertical flux. The fact that according to Eq. (6) countergradient fluxes cause a destruction of variance offers a likely explanation for the smaller length scales for these cases.

Appendix: Model initialization

During 1 to 19 July 1987 sixty-nine vertical profiles of the temperature and the relative humidity were measured by radiosondes. From these data mean vertical profiles for the potential temperature and specific humidity were calculated by Duynkerke and Teixeira (2001), which are shown in Figure 2. Because the inversion height is quite variable in time the inversion structure is smeared out in the averaged profile. To quantify the strength of the inversion the jumps in liquid water potential temperature and total water content were estimated from each individual sounding as well. This was done in a method similar to Kuo and Schubert (1988). For each of the soundings we determined the cloud-top jump in total water

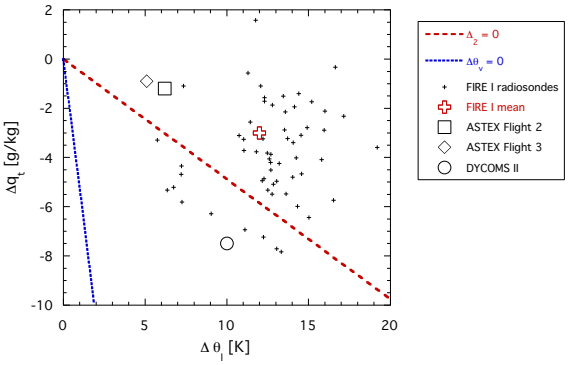

Figure 10: The $(\Delta\theta_l, \Delta q_t)$ plane. It shows the thermodynamic instability curve for the clear convective boundary layer $\Delta\theta_v$ = 0 and the cloud-top instability criterion proposed by Randall (1980) and Deardorff (1980), Δ_2 = 0. Plotted are sixty-two points obtained from high vertical resolution soundings taken from 30 June to 19 July 1987 on San Nicolas island. Also shown are the mean inversion jumps of stratocumulus cases that have been used for other intercomparison cases: Flights 2 and 3 of the ASTEX First Lagrangian (De Roode and Duynkerke, 1997) and Flight RF01 of DYCOMS II (Stevens et al., 2003). The linestyles and symbols are according to the legend.

Δq_t as follows. First the height of the inversion base was determined from the level above which the potential temperature strongly increases with height. Next, we computed the vertically averaged specific humidity in the layer 200 m above the inversion. Finally, we substracted from this the average specific humidity in the layer which extends from 65 to 165 m above sea level (the island sounding site being 38 m above sea level). If the boundary layer is vertically well mixed the specific humidity difference should be equivalent to the jump in total water at cloud top. The procedure for $\Delta\theta_l$ is identically done with θ. In this way each sounding is characterized by a point in the $(\Delta\theta_l, \Delta q_t)$ plane as shown in Figure 10. The average jump at cloud top is given by $\Delta\theta_l$ = 12 K and Δq_t = -3.0 $g\,kg^{-1}$.

In the boundary layer ($0 < z \leq 595$ m) the initial vertical profiles for liquid water potential temperature ($\theta_l = 287.5$K) and total water content ($q_t = 9.6 g\,kg^{-1}$), and above the boundary layer ($595 < z \leq$

1200m)

$$\theta_l = 299.5 + 0.0075(z - 595)K \quad (7)$$

$$q_t = 6.6 - 0.003(z - 595)g\,kg^{-1} \quad (8)$$

A comparison of the monthly mean values with observed vertical profiles during 14 and 15 July indicates that in the free atmosphere the total water contents are nearly the same, but the monthly mean potential temperature is about 5 K colder. The initial total water content in the boundary layer is set to a value that is close to the observations during 14 and 15 July, in order to give an initial cloud-base height of about $250m$.

The initial wind fields were set to the geostrophic winds

$$(u, v) = U_g(\cos\,\alpha_g, \sin\,\alpha_g). \quad (9)$$

with $U_g = 6.0ms^{-1}$ and $\alpha_g = 305°$. The surface temperature and pressure are prescribed as $T_s = 289.0K$ and $p_s = 1012.5hPa$, respectively (Duynkerke and Teixeira, 2001). Because the wind is blowing almost parallel to the isotherms of the sea surface temperature this means that the surface temperature hardly changes as the air flows south-eastwards (Duynkerke and Hignett, 1993). The specific humidity at the sea-surface is set to its saturated value at the sea-surface temperature, $q_s = 11.1g\,kg^{-1}$. The surface roughness length is set to $2 \times 10^{-4}m$, and the Coriolis parameter $f = 8.0 \times 10^{-5}s^{-1}$ $(33.3°N, 119.5°W)$.

The large-scale subsidence rate $\overline{w}$ is prescribed as,

$$\overline{w} = -1 \times 10^{-5}z \quad ms^{-1}. \quad (10)$$

It is hard to obtain the large-scale subsidence rate directly from observations. The subsidence rate in Eq. (10) is based on test simulations with the IMAU LES model, and approximately balances the diurnally-averaged entrainment rate. Eq. (10) gives subsidence rates that are nearly a factor of two larger than the average values over San Nicholas Island presented by Neiburger (1960).

To balance the subsidence heating and drying above the boundary layer a large-scale (LS) advection term is included in the simulation:

$$\left(\frac{d\theta_l}{dt}\right)_{LS} = -7.5 \times 10^{-8}\,\max(z, 500), \quad (11)$$

$$\left(\frac{dq_t}{dt}\right)_{LS} = 3.0 \times 10^{-11}\,\max(z, 500), \quad (12)$$

with units Ks^{-1} and $kg\,kg^{-1}\,s^{-1}$, respectively. In the boundary layer the large-scale horizontal advection tendencies approximately counteract the divergence of the turbulent fluxes of heat and moisture. The u, v, θ_l and q_t profiles in the damping layer are relaxed towards the geostrophic wind and initial thermodynamic profiles (8) and (9), respectively.

The net upward longwave radiation is parametrized as:

$$F_l(z) = \Delta F_t e^{-a\,LWP(z,z_t)}, \quad (13)$$

where $\Delta F_t = 70Wm^{-2}$ (Duda et al., 1991) is the longwave radiative flux divergence at the cloud top, $a = 130m^2\,kg^{-1}$ a constant, $z_t = 1200m$ the top of the model domain.

The solar radiation is a function of the solar zenith angle θ_0 ($\mu_0 = \cos\theta_0$) and the optical depth τ which is parametrized as:

$$\tau(z) = \frac{3}{2}\frac{LWP(z, z_t)}{r_e\rho_l} \quad (14)$$

where $r_e = 10\mu m$ is the effective radius and $\rho_l = 1000kg\,m^{-3}$ is the density of water. The net downward shortwave radiation F_s is obtained from the analytical solution of the delta-Eddington approximation. The removal of liquid water by precipitation was not taken into account.

In total six LES models and ten SCMs have participated in this study. Periodic lateral boundary conditions were applied to the LES models. A spatially uncorrelated random perturbation between -0.1 and 0.1 K was applied to the initial temperature field at all grid points. Throughout the domain an initial value for sub-grid TKE of 1 m^2s^{-2} was specified. The grid size in the horizontal is 50 m and in the vertical 10 m, covering a domain of 2.5 km in x and y and 1.2 km in z.

Acknowledgement The investigations were supported by the Netherlands Organization for Scientific Research (NWO). This work was sponsored by the National Computing Facilities Foundation (NCF) for the use of supercomputer facilities.

References

Albrecht, B. A., C. W. Fairall, D. W. Thomson, A. B. White, J. B. Snider, and W. H. Schubert, 1990: Surface-based remote sensing of the observed and the adiabatic liquid water content of stratocumulus clouds. *grl*, **17**, 89–92.

Albrecht, B. A., D. A. Randall, and S. Nicholls, 1988: Observations of marine stratocumulus clouds during FIRE. *Bull. Am. Meteorol. Soc.*, **69**, 618–626.

Bretherton, C. S., T. Uttal, C. W. Fairall, S. Yuter, R. Weller, D. Baumgardner, K. Comstock, R. Wood, and G. Raga, 2004: The EPIC 2001 stratocumulus study. *Bull. Amer. Meteor. Soc., in press*.

Cahalan, R. F., W. Ridgway, W. J. Wiscombe, S. Gollmer, and Harshvardhan, 1994: Independent pixel and Monte-Carlo estimates of stratocumulus albedo. *J. Atmos. Sci.*, **51**, 3776–3790.

Cahalan, R. F. and J. B. Snider, 1989: Marine stratocumulus structure. *Remote Sensing Environ.*, **28**, 95–107.

De Roode, S. R. and P. G. Duynkerke, 1997: Observed Lagrangian transition of stratocumulus into cumulus during ASTEX: Mean state and turbulence structure. *J. Atmos. Sci.*, **54**, 2157–2173.

De Roode, S. R., P. G. Duynkerke, and H. J. J. Jonker, 2004a: Large eddy simulation: How large is large enough? *J. Atmos. Sci.*, **61**, 403–421.

De Roode, S. R., H. J. J. Jonker, P. G. Duynkerke, and B. Stevens, 2004b: Countergradient fluxes of conserved variables in the clear convective and stratocumulus-topped boundary layer: The role of the entrainment flux. *Boundary-Layer Meteorol.*, **112**, 179–196.

Deardorff, J. W., 1980: Cloud-top entrainment instability. *J. Atmos. Sci.*, **37**, 131–147.

Duda, D. P., G. L. Stephens, and S. K. Cox, 1991: Microphysical and radiative properties of marine stratocumulus from tethered balloon measurements. *J. Appl. Meteorol.*, **30**, 170–186.

Duynkerke, P. G., S. R. de Roode, M. C. van Zanten, J. Calvo, J. Cuxart, S. Cheinet, A. Chlond, H. Grenier, P. J. Jonker, M. Köhler, G. Lenderink, D. Lewellen, C.-L. Lappen, A. P. Lock, C.-H. Moeng, F. Müller, D. Olmeda, J.-M. Piriou, E. Sanchez, and I. Sednev, 2004: Observations and numerical simulations ofthe diurnal cycle of the eurocs stratocumulus case. *Accepted for publication in the Q. J. R. Met. Soc. EUROCS special issue*.

Duynkerke, P. G. and P. Hignett, 1993: Simulation of diurnal variation in a stratocumulus-capped marine boundary layer during FIRE. *Mon. Weather Rev.*, **121**, 3291–3300.

Duynkerke, P. G. and J. Teixeira, 2001: Comparison of the ECMWF reanalysis with FIRE I observations: Diurnal variation of marine stratocumulus. *J. Climate*, **14**, 1466–1478.

Hignett, P., 1991: Observations of the diurnal variation in a cloud-capped marine boundary layer. *J. Atmos. Sci.*, **48**, 1474–1482.

Jonker, H. J. J., P. G. Duynkerke, and J. W. M. Cuijpers, 1999: Mesoscale fluctuations in scalars generated by boundary layer convection. *J. Atmos. Sci.*, **56**, 801–808.

Klein, S. A. and D. L. Hartmann, 1993: The seasonal cycle of low stratiform clouds. *J. Climate*, 1587–1606.

Kuo, H. and W. H. Schubert, 1988: Stability of cloud-topped boundary layers. *Q. J. R. Meteorol. Soc.*, **114**, 887–917.

Los, A. and P. G. Duynkerke, 2001: Parametrization of solar radiation in inhomogeneous stratocumulus: Albedo bias. *Q. J. R. Meteorol. Soc.*, **127**, 1593–1614.

Moyer, K. A. and G. S. Young, 1994: Observations of mesoscale cellular convection from the marine stratocumulus phase of FIRE. *Boundary-Layer Meteorol.*, **71**, 109–133.

Neiburger, M., 1960: The relation of air mass structure to the field of motion over the eastern North Pacific Ocean in summer. *Tellus*, **12**, 31–40.

Nicholls, S., 1984: The dynamics of stratocumulus: Aircraft observations and comparisons with a mixed layer model. *Q. J. R. Meteorol. Soc.*, **110**, 783–820.

Norris, J. R., 1997a: Low cloud type over the ocean from surface observations. Part I: Relationship to surface meteorology and the vertical distribution of temperature and moisture. *J. Climate*, **11**, 369–382.

— 1997b: Low cloud type over the ocean from surface observations. Part II: Geographical and seasonal variations. *J. Climate*, **11**, 383–403.

Randall, D. A., 1980: Conditional instability of the first kind upside down. *J. Atmos. Sci.*, **37**, 125–130.

Stevens, B., D. H. Lenschow, I. Faloona, C.-H. Moeng, D. K. Lilly, B. Blomquist, G. Vali, A. Bandy, T. Campos, H. Gerber, S. Haimov, B. Morley, and D. Thorton, 2003: On entrainment rates in nocturnal marine stratocumulus. *Submitted for publication in the Q. J. Roy. Met. Soc.*.

Stull, R. B., 1988: *An Introduction to Boundary Layer Meteorology*. Kluwer Academic Publishers, 666 pp.

Wood, R. and P. R. Field, 2000: Relationships between total water, condensed water, and cloud fraction in stratiform clouds examined using aircraft data. *J. Atmos. Sci.*, **57**, 1888–1905.